

Monte Carlo Study of Ferromagnetism in (III,Mn)V Semiconductors

John Schliemann, Jürgen König, and A. H. MacDonald

Department of Physics, The University of Texas, Austin, TX 78712

Department of Physics, Indiana University, Bloomington, IN 47405

(May 20, 2019)

We report on Monte Carlo studies of the kinetic exchange model for (III,Mn)V ferromagnetic semiconductors in which $S = 5/2$ local moments, representing Mn^{2+} ions, are exchange coupled to band electrons. We treat the Mn^{2+} spin orientations as classical degrees of freedom and use the Hybrid Monte Carlo algorithm to explore thermodynamically important Mn spin configurations. The critical temperature T_c of the model is unambiguously signalled in our finite-size simulations by pronounced peaks in fluctuations of both Mn and band carrier total spins. The T_c 's we obtain are, over much of the model's parameter space, substantially smaller than those estimated using mean-field theory. When mean-field theory fails, short-range magnetic order and finite *local* carrier spin polarisation are present for temperatures substantially larger than T_c . For the simplest version of the model, which has a single parabolic band with effective mass m^* , the dependence of T_c on m^* is sublinear at large masses, in disagreement with the mean-field theory result $T_c \propto m^*$. For the carrier densities studied, results obtained with a six-band Luttinger model band Hamiltonian are in good agreement with those obtained for a model with a single parabolic band whose effective mass is equal to the Kohn-Luttinger model heavy-hole mass.

PACS numbers: 75.70.Dd, 75.40.Mg, 75.40.Cx

I. INTRODUCTION

Diluted magnetic semiconductors have long attracted attention [1], partly because their electronic properties are very sensitive to external magnetic fields. The discovery of ferromagnetism at comparatively high temperatures ($T_c > 100\text{K}$) in Mn-doped (III,V) semiconductors [2,3] has intensified interest, partly because of the new technological pathways that might be opened if room temperature ferromagnetism were achieved in a semiconductor with favorable materials properties [4,5]. The search for materials in this class with higher ferromagnetic transition temperatures, and the effort to achieve a deeper understanding of all physical property trends, has stimulated a large body of experimental and theoretical research.

To date, most theoretical work [6–8] has been based on kinetic exchange models of the type used here and detailed below. First principles density-functional-theory electronic structure calculations [9,10] are qualitatively in accord with these phenomenological models, although more work may be necessary to reliably judge the accuracy for these materials of the local-spin-density ap-

proximation before they can be used to guide model refinement. The model's low-energy degrees of freedom are $S = 5/2$ spins representing Mn^{2+} ions and holes in the semiconductor valence band that are free to move through the system. Ferromagnetism is most easily discussed in a Mn continuum version of the model, justified in part by the small ratio of hole density to Mn ion density in experimental systems [6–8]. The constant Mn density model is somewhat analogous to the jellium model for metals in that it artificially preserves translational invariance. In this approximation, the ground state is always ferromagnetic because the exchange energy gained by polarizing is linear in the hole-spin density whereas the band and hole-hole interaction energy cost is quadratic. The critical temperature T_c and other magnetic properties of the continuum model are relatively easily evaluated using a mean-field approximation that considers only spatially constant configurations of the Mn-spin-orientation field [6–8]. It appears that the resulting predictions for T_c , magnetic anisotropy, optical absorption, and other properties are often at least qualitatively in accord with experiment, although further experimental and theoretical work is needed to confidently establish where this approach is and is not reliable.

It is well known that mean-field theories tend to overestimate the stability of ordered phases, because they fail to account for thermal and quantum fluctuations that can destroy long-range order. In particular, they predict critical temperatures which are systematically too high. A step toward a more complete description of ferromagnetism in diluted magnetic semiconductors was taken in Ref. [11], where a theory of collective spin-wave excitations was developed for the continuum version of the kinetic-exchange model. T_c estimates [12] based on this theory of the ferromagnet's spin stiffness establish that mean-field theory becomes less reliable for stronger exchange coupling and for flatter semiconductor valence bands; the higher the predicted T_c the lower the reliability. The approximate collective-fluctuation T_c bounds proposed in Ref. [12] are based on $T = 0$ spin-wave energies of the continuum version of the kinetic exchange model. The considerations of this paper demonstrate that collective magnetization fluctuations will dominate in a part of the model-parameter range relevant to ferromagnetic semiconductors. In this work we report on Monte Carlo simulations, using a Hybrid Monte Carlo algorithm [13], that fully account for thermal fluctuations of Mn spin orientations and shed further light on the finite-temperature properties of the kinetic-exchange

model. Some of the results of these calculations were described briefly in Ref. [12]. In this paper we give a complete description of the calculations, including all important technical details. In addition, we also present results obtained using a realistic six-band $\vec{k} \cdot \vec{p}$ model for the valence bands of zincblende semiconductors, allowing us to assess the importance for thermal fluctuations of band structure details. A related Monte Carlo study by Sakai *et al.* [14] has the same motivation as ours, but examines a model of Ising localized spins coupled to band electrons that has gapped collective excitations and qualitatively different thermodynamic properties.

Our simulations are directed toward the regime of Mn concentration in $\text{III}_{1-x}\text{Mn}_x\text{V}$ alloys where the highest ferromagnetic transition temperatures have been observed, $x \sim 0.05$ [3]. In this regime the heavily-doped semiconductors are strongly disordered three-dimensional metals with $k_F \ell \sim 3$. (Here k_F is a typical Fermi wavevector and ℓ is a mean-free path estimated from the measured $T = 0$ resistivity.) The sources of disorder in these alloys have not been fully cataloged, although randomness in the Mn alloy positions and antisite defects (group V elements on group III sites) are almost certainly among them. In our simulations we include only the former disorder source. In the continuum version of the model this source is absent and the system is disorder-free. We find that disorder has quantitative but not qualitative importance. Randomness in the Mn ion distribution will be increasingly important at lower Mn concentrations, particularly on the insulating side of the metal insulator transition which occurs for $x \sim 0.02$, and has an overriding importance in the models studied in Ref. [15] that are directed to the dilute Mn concentration limit. In the extreme dilute limit, all holes are bound to Mn^{2+} acceptors, forming neutral complexes. For small Mn concentrations, holes may hop from acceptor site to acceptor site, but it is still useful to regard them as belonging to an impurity band. On the metallic side of the metal insulator transition, the concept of an impurity band is less useful and the host semiconductor band structure has to be modelled realistically, as in the present work. In order to correctly capture the physics of the dilute limit in our more general calculations we would need to include Coulombic interactions between Mn ions and valence band spins in addition to exchange interactions. In a ground state or mean-field calculation this would not be an essential complication. Here, however, if Coulomb interactions were explicitly included, we would have to self-consistently solve for the valence band electron screening charges for each Mn spin configuration, or adopt a Car-Parrinello [16] type of scheme. In ignoring Coulomb interactions, we take the view that in the regime of interest to us, well on the metallic side of the metal-insulator transition, screened Coulomb interactions are much less important than strong unscreened exchange interactions in weighting different Mn spin configurations.

This paper is organized as follows: In section II we discuss the kinetic-exchange model of Mn-doped (III,V) semiconductors. In section III we summarize the main features of the Hybrid Monte Carlo algorithm that are important for our purposes. Numerical results obtained by this method as well as a detailed discussion of important technical aspects are presented in section IV. Our data show very clearly the typical features of ferromagnetic transitions signalled unambiguously by susceptibility peaks. We discuss the critical temperature as a function of effective mass, carrier density, and exchange-coupling strength. We close with a summary in section V.

II. THE MODEL

We now describe the kinetic-exchange model we use for (III,Mn)V diluted magnetic semiconductor ferromagnets in detail. In this material class, the highest critical temperature of 110K has been obtained for $\text{Ga}_{1-x}\text{Mn}_x\text{As}$ with $x \approx 0.05$ [3]. The manganese ions are assumed to be Mn^{2+} with a $3d^5$, $S = 5/2$ configuration, and to be placed at random on group III element sites so that they are acceptors. The concentration of holes is, however, allowed to differ from the Mn concentration, since the system is strongly compensated by anti-site defects, i.e. group V atoms on group III sites. In practice the hole concentration is often not accurately known; its determination from Hall effect measurements is complicated by the extraordinary Hall effect that occurs in all ferromagnetic metals.

Long range magnetic order occurs in this dilute system of magnetic moments because of an exchange interaction between the spins of the manganese ions and spins of the valence band holes. The minimal model to describe this carrier-induced ferromagnetism is

$$\mathcal{H} = \sum_i \frac{\vec{p}_i^2}{2m^*} + \sum_I \int d^3r J(\vec{r} - \vec{R}_I) \vec{s}(\vec{r}) \cdot \vec{S}_I. \quad (1)$$

This Hamiltonian describes noninteracting carriers in a parabolic band characterized by an effective mass m^* , whose spin density $\vec{s}(\vec{r})$ is coupled to manganese ion spins \vec{S}_I at locations \vec{R}_I by an antiferromagnetic exchange coupling. To account for the finite extent of the manganese ions, the exchange is modelled by a spatially extended coupling $J(\vec{r})$ [17]; we use a Gaussian centered around the ion position,

$$J(\vec{r}) = \frac{J_{pd}}{(2\pi a_0^2)^{\frac{3}{2}}} e^{-\frac{r^2}{2a_0^2}}. \quad (2)$$

Both the strength and range of this interaction are phenomenological parameters to be fixed by comparison with experiment or, ideally, to be extracted from first principles electronic structure calculations. The exchange-coupling range parameter a_0 in Eq. (2) is required in our

calculations to keep exchange-coupling shifts in quasi-particle energies finite. In the numerical studies to be presented below we usually choose $a_0 = 0.1\text{nm}$, which appears to be a reasonable value for the d-ion radius in $\text{Ga}_{1-x}\text{Mn}_x\text{As}$, whose lattice constant is $\sim 0.60\text{nm}$ [2,3]. However, we will see that properties of the system depend only very weakly on a_0 , as long as this quantity is not increased to large values.

The exchange parameter $J_{pd} > 0$ characterizes the strength of the exchange interaction between carriers and manganese ions. Typical experimental values for this quantity are of the order of 0.1eVnm^3 . (The pd subscript on the coupling constant is a reminder of its presumed physical origin in the hybridization of valence-band p-orbitals and Mn-ion d-orbitals. Since the carrier spin density $\vec{s}(\vec{r})$ has dimension 1/volume and \vec{S}_I is dimensionless, J_{pd} has the dimension of energy times volume.)

We emphasize that the interaction in Eq. (1) is of the isotropic Heisenberg type. In a parabolic band model, total energies are therefore invariant under global rotations of all Mn spins and slow variations in orientation have a small energy cost. Even with the realistic band models discussed below, the energy cost of global Mn spin rotations is still very small [7]. Models with Ising-like interactions [14] *do not* capture this essential element of (III,Mn)V ferromagnet physics, although they are much more easily studied.

An important refinement of the above model, Eq. (1), is obtained by replacing the single parabolic band by a realistic model for the host semiconductor valence bands. In the materials of interest these derive from atomic p-orbitals and have a spin-orbit coupling strength that exceeds the Fermi energy. Importantly, eigenstates do not have definite angular momentum quantum numbers at finite wavevector; at the center of the Brillouin zone, however, they have definite total angular momentum $J \in \{3/2, 1/2\}$. We use these states in a $\vec{k} \cdot \vec{p}$ scheme, choosing as basis states [18,7]

$$\begin{aligned}
|1\rangle &: = \left|\frac{3}{2}, \frac{3}{2}\right\rangle = |1, \uparrow\rangle \\
|2\rangle &: = \left|\frac{3}{2}, -\frac{1}{2}\right\rangle = \frac{1}{\sqrt{3}}|-1, \uparrow\rangle + \sqrt{\frac{2}{3}}|0, \downarrow\rangle \\
|3\rangle &: = \left|\frac{3}{2}, \frac{1}{2}\right\rangle = \frac{1}{\sqrt{3}}|1, \downarrow\rangle + \sqrt{\frac{2}{3}}|0, \uparrow\rangle \\
|4\rangle &: = \left|\frac{3}{2}, -\frac{3}{2}\right\rangle = |-1, \downarrow\rangle \\
|5\rangle &: = \left|\frac{1}{2}, \frac{1}{2}\right\rangle = -\frac{1}{\sqrt{3}}|0, \uparrow\rangle + \sqrt{\frac{2}{3}}|1, \downarrow\rangle \\
|6\rangle &: = \left|\frac{1}{2}, -\frac{1}{2}\right\rangle = \frac{1}{\sqrt{3}}|0, \downarrow\rangle - \sqrt{\frac{2}{3}}|-1, \uparrow\rangle.
\end{aligned} \tag{3}$$

Near the Brillouin-zone center, the band structure can be parameterized by a small number of symmetry-adapted parameters of the Kohn-Luttinger Hamiltonian [19,18,7]). In the above basis this effective kinetic-energy

operator reads

$$\mathcal{H}_{KL} = \begin{pmatrix} \mathcal{H}_{hh} & -c & -b & 0 & \frac{b}{\sqrt{2}} & c\sqrt{2} \\ -c^* & \mathcal{H}_{lh} & 0 & b & -\frac{b^*\sqrt{3}}{\sqrt{2}} & -d \\ -b^* & 0 & \mathcal{H}_{lh} & -c & d & -\frac{b\sqrt{3}}{\sqrt{2}} \\ 0 & b^* & -c^* & \mathcal{H}_{hh} & -c^*\sqrt{2} & \frac{b^*}{\sqrt{2}} \\ \frac{b^*}{\sqrt{2}} & -\frac{b\sqrt{3}}{\sqrt{2}} & d & -c\sqrt{2} & \mathcal{H}_{so} & 0 \\ c^*\sqrt{2} & -d & -\frac{b^*\sqrt{3}}{\sqrt{2}} & \frac{b}{\sqrt{2}} & 0 & \mathcal{H}_{so} \end{pmatrix} \tag{4}$$

where the entries of this 6×6 matrix for each wavevector \vec{k} are given by

$$\begin{aligned}
\mathcal{H}_{hh} &= \frac{\hbar^2}{2m} [(\gamma_1 + \gamma_2)(k_x^2 + k_y^2) + (\gamma_1 - 2\gamma_2)k_z^2] \\
\mathcal{H}_{lh} &= \frac{\hbar^2}{2m} [(\gamma_1 - \gamma_2)(k_x^2 + k_y^2) + (\gamma_1 + 2\gamma_2)k_z^2] \\
\mathcal{H}_{so} &= \frac{\hbar^2}{2m} \gamma_1 (k_x^2 + k_y^2 + k_z^2) + \Delta_{so} \\
b &= \frac{\sqrt{3}\hbar^2}{m} \gamma_3 k_z (k_x - ik_y) \\
c &= \frac{\sqrt{3}\hbar^2}{2m} [\gamma_2 (k_x^2 - k_y^2) - 2i\gamma_3 k_x k_y] \\
d &= -\frac{\sqrt{2}\hbar^2}{2m} \gamma_2 [2k_z^2 - (k_x^2 + k_y^2)].
\end{aligned} \tag{5}$$

The quantities $\gamma_1, \gamma_2, \gamma_3$ are called Luttinger parameters, m is the bare electron mass, and Δ_{so} is the spin-orbit coupling which splits the six states at the valence band edge into a doublet and a quartet. These band parameters are accurately known for a large number of (III,V) compound semiconductors [20]. For all numerical calculations we use $(\gamma_1, \gamma_2, \gamma_3) = (6.85, 2.1, 2.9)$ and $\Delta_{so} = 0.34\text{eV}$, the band parameter set appropriate for GaAs.

In the kinetic-exchange model with realistic band structure, the Hamiltonian (4) replaces the kinetic part of Eq. (1). The Hilbert space dimension of the one-particle problem is, thus, enlarged by a factor of three. The Kohn-Luttinger Hamiltonian has already been adopted in some mean-field calculations for the continuum kinetic exchange model [6,7]. This realistic description is essential if important magnetic parameters connected with magnetocrystalline anisotropy and anisotropic magnetoresistance are to be addressed.

The material $\text{Ga}_{1-x}\text{Mn}_x\text{As}$ has a zincblende structure, in which the cations and anions each form an fcc lattice. In the alloy manganese ions are located on randomly chosen cation sites, forming a disordered system of local moments. In an approximation consistent with our band Hamiltonians we ignore the underlying lattice and place the ions positions completely at random within periodically continued cubic simulation cells. In the Monte Carlo calculations described below, we average over different disorder realisations. However, we find that the re-

sults of different realizations typically lie within a range of a few percent.

In our simulations we treat the $S = 5/2$ Mn spins as classical degrees of freedom. This approximation is not severe even in a mean-field theory where it alters the critical temperature by a factor of $1 + 1/S = 1.4$. It is even less important in the common circumstance where the most important spin fluctuations are collective. This classical approximation is, therefore, a less serious source of uncertainty in our representation of (III,Mn)V ferromagnet thermodynamics than the modelling issues discussed above; in our judgement the substantially greater complexity of quantum calculations is not warranted at present. Thus, the state of each ion spin \vec{S}_I is specified by two polar angles ϑ_I, φ_I . In interpreting results, however, it is important to realize that some low-temperature power laws will be altered by quantum freeze out.

We are interested in thermal expectation values of the form

$$\bar{f} = \frac{1}{\mathcal{Z}} \int_0^{2\pi} d\varphi \int_0^\pi d\vartheta \sin \vartheta \text{Tr} \left\{ \hat{f}(\vartheta, \varphi) e^{-\beta \mathcal{H}} \right\}, \quad (6)$$

where β is the inverse temperature, \mathcal{Z} the partition function, and ϑ, φ are shorthand notations for the whole set of classical spin coordinates. The quantity $\hat{f}(\vartheta, \varphi)$ is a function of the ion spin angles and an operator with respect to the quantum mechanical carrier degrees of freedom over which the trace is performed. In practice we replace the fermion trace by a ground state expectation value, since the temperatures of interest will always be much smaller than the Fermi energy. For typical carrier densities n of order 0.1 nm^{-3} , the Fermi temperature for the carriers is $\gtrsim 1000 \text{ K}$, compared to ferromagnetic critical temperatures $\sim 100 \text{ K}$. Thermal effects in the carrier system are therefore negligible. Thus,

$$\bar{f} = \frac{1}{\mathcal{Z}} \int_0^{2\pi} d\varphi \int_0^\pi d\vartheta \sin \vartheta \langle 0 | \hat{f}(\vartheta, \varphi) | 0 \rangle e^{-\beta \langle 0 | \mathcal{H} | 0 \rangle}, \quad (7)$$

where $|0\rangle$ denotes the ground state of non-interacting fermions with the appropriate band Hamiltonian and a Zeeman-coupling term h whose effective magnetic field B_{eff} is due to exchange interactions with the localized spins,

$$h = - \int d^3 r \vec{s}(\vec{r}) \cdot \vec{B}_{\text{eff}}(\vec{r})$$

$$\vec{B}_{\text{eff}}(\vec{r}) = - \sum_I J(\vec{r} - \vec{R}_I) S \hat{\Omega}_I \quad (8)$$

where $\hat{\Omega}_I = (\sin(\theta_I) \cos(\phi_I), \sin(\theta_I) \sin(\phi_I), \cos(\theta_I))$ is the direction of the classical spin at \vec{R}_I . In the following we denote thermal expectation values of quantities defined in terms of classical spin orientation variables by $\langle \cdot \rangle$ and quantum mechanical expectation values within the carriers ground state by $\langle 0 | \cdot | 0 \rangle$. The latter quantities will be averaged also thermally according to Eq. (7).

III. THE HYBRID MONTE CARLO ALGORITHM

A standard way to evaluate expectation values of the form Eq. (7) is to use classical Monte Carlo algorithms which perform a random walk in the phase space of the classical variables (ϑ, φ) . The probabilities governing this Monte Carlo dynamics are specified by the dependence of many-fermion energy on the localized-spin configuration. The many-fermion ground state is a Slater determinant whose single-particle orbitals are the lowest energy eigenstates of a single-band or multi-band Hamiltonian of the form (1). For the case of a parabolic band, the matrix elements of the corresponding one-particle Hamiltonian in a plane-wave basis read

$$\langle \vec{k}' \sigma' | \mathcal{H} | \vec{k} \sigma \rangle = \frac{\hbar^2 k^2}{2m^*} \delta_{\vec{k}, \vec{k}'} \delta_{\sigma, \sigma'} + \frac{S}{2L^3} \sum_I J(\vec{k} - \vec{k}') e^{i(\vec{k} - \vec{k}') \cdot \vec{R}_I} \hat{\Omega}_I \cdot \vec{\tau}_{\sigma, \sigma'}, \quad (9)$$

where \vec{k} and σ denote wavevector and spin indices, respectively, $J(\vec{k})$ is the Fourier transform of $J(\vec{r})$, and L the edge length of the simulation cube. Periodic boundary conditions restrict the admissible values of wavevector components to integer multiples of $2\pi/L$. In Eq. (9) $\vec{\tau}$ is the vector of Pauli spin matrices.

Since the many-particle groundstate of the carrier system has to be computed at each Monte Carlo step, the computational effort required for the present calculations is much larger than in simple classical spin models. In the usual Metropolis algorithm, a single spin orientation is altered at each step. If this algorithm were employed here the time required to diagonalize the single-particle Hamiltonian each time would severely limit the efficiency of the algorithm. We therefore use the Hybrid Monte Carlo algorithm, which was introduced in the mid 1980's in the context of lattice field theories [13]. In this method *all* classical variables are altered in one Monte Carlo step. This drastically reduces the number of matrix diagonalisations required to explore statistically important magnetic configurations. The Hybrid algorithm is a powerful method for Monte Carlo simulations in systems containing coupled classical and quantum mechanical degrees of freedom. Very recently, a variant of this algorithm has been applied to a system of classical degrees of freedom coupled to non-interacting lattice fermions [21], a problem similar to the one studied here.

The Hybrid Monte Carlo algorithm determines average values defined in terms of a probability distribution P of the form

$$P(\phi) \propto e^{-\mathcal{S}(\phi)}. \quad (10)$$

The “action” \mathcal{S} depends on a set of classical variables summarized by the symbol ϕ . The basic trick of the algorithm is to introduce a “fake dynamics” for the classical variables which is governed by the “fake Hamiltonian”

$$H' = \frac{1}{2}\pi^2 + \mathcal{S}'(\phi) \quad (11)$$

with “fake momenta” π and an action \mathcal{S}' which is not necessarily identical to \mathcal{S} .

In this algorithm one Monte Carlo step is performed in the following way: (i) Choose a value for each fake momentum from its Gaussian distribution. (ii) Let the system evolve in Monte Carlo time τ according to the Hamilton equations of motions,

$$\partial_\tau \phi = \frac{\partial H'}{\partial \pi} = \pi \quad , \quad \partial_\tau \pi = -\frac{\partial H'}{\partial \phi} = -\frac{\partial \mathcal{S}'}{\partial \phi} \quad , \quad (12)$$

which leads to a new configuration of fields and fake momenta (ϕ', π') . (iii) Accept this new configuration with a probability

$$\min\{1, \exp[H(\phi, \pi) - H(\phi', \pi')]\} \quad , \quad (13)$$

where H is the “true Hamiltonian”,

$$H = \frac{1}{2}\pi^2 + \mathcal{S}(\phi) \quad . \quad (14)$$

This acceptance condition is reminiscent of the Metropolis algorithm. We note that the acceptance probability is strictly unity for $\mathcal{S} = \mathcal{S}'$, and that the acceptance rate in this Monte Carlo procedure reflects the difference between the two actions \mathcal{S} and \mathcal{S}' .

Thermodynamic averages are calculated using

$$\bar{f} = \frac{1}{N} \sum_{n=1}^N \langle 0_n | \hat{f}(\vartheta_n, \varphi_n) | 0_n \rangle \quad , \quad (15)$$

where n labels the accepted configurations. As shown in Ref. [13] this Hybrid Monte Carlo algorithm generates a Markov chain which converges to the distribution (10).

Our calculations adopt this scheme for the set of classical spin angles and the action

$$\mathcal{S} = \beta \langle 0 | \mathcal{H} | 0 \rangle - \sum_I \ln |\sin \vartheta_I| \quad . \quad (16)$$

The first term is the energy of the carrier system for a given classical spin configuration and the logarithms arise from the Jacobi determinant in Eq. (7). Note that this part is not multiplied by the inverse temperature β .

As pointed out above, the action \mathcal{S}' need not to be the same as \mathcal{S} . In our calculation, we use this freedom to reduce the computational effort. Our fake action \mathcal{S}' is defined as in Eq. (16) but for an itinerant-carrier state $|0\rangle_i$ that is evaluated in the beginning of each Monte Carlo step and taken to be fixed in the subsequent integration of the fake dynamics (12). In addition, we replace $J(\vec{r})$ by $J_{pd}\delta(\vec{r})$, i.e., we use the $a_0 \rightarrow 0$ limit of the exchange coupling for the fake dynamics. The force term in the effective dynamics is then readily evaluated from

$$\frac{\partial \langle i | 0 | \mathcal{H} | 0 \rangle_i}{\partial \Omega_I} = JS \left(\langle i | 0 | \vec{s}(\vec{R}_I) | 0 \rangle_i \right) \quad . \quad (17)$$

In the fake dynamics the localized spins move under the influence of the fixed effective magnetic fields generated by exchange interactions with the fixed electronic spins of $|0\rangle_i$. With this approach, only one matrix diagonalization is required to update all Mn spin orientations. However, since the acceptance probability (13) is determined by the action \mathcal{S} , the sampling is still performed with respect to the original distribution (10). The choice of \mathcal{S}' being different from \mathcal{S} is, therefore, not an approximation as long as the Hamiltonian fake dynamics is reversible, a feature which can be incorporated in the numerical integration using the leapfrog algorithm [13].

The action (16) becomes singular if one of the polar angles ϑ is equal to an integer multiple of π . This may lead, in principle, to difficulties in the numerical implementation of our method. But since this singularity is only logarithmic, and since in the fake dynamics (12) the ϑ 's are repelled from the singular points, we have never encountered any practical difficulty due to these coordinate singularities.

IV. NUMERICAL RESULTS

In this section we present our numerical results. We concentrate on the spin polarizations of the manganese ions and the carriers as a function of temperature and address the ferromagnetic transition. We start with the case of parabolic bands described by the Hamiltonian (1).

A. Parabolic bands

In the following we present results in dimensionful units for parameters in the range of interest for (Ga,Mn)As. It is hoped that ferromagnetism will be realized in other materials described by the same model but with different parameter values. In this connection, it is useful to observe that band and exchange interaction terms in our model Hamiltonian both scale simply with changes in length scale and model parameters. Results for the parabolic band model have a non-trivial dependence only on the ratio of the density n band carriers and the concentration of Mn ions N , and on the ratio of exchange interaction and band energy scales, Δ/ϵ_F . Here $\Delta = J_{pd}NS$ is the continuum model mean-field-theory band exchange splitting, and $\epsilon_F/k_B = T_F \approx 4230\text{K}(m/m^*)(n[\text{nm}^{-3}])^{2/3}$ is the band Fermi energy in the paramagnetic state. There is also a very weak dependence on the dimensionless range of the exchange interaction $a_0N^{1/3}$, that does not play an important role and will usually be ignored.

In the following subsections we first show some typical numerical results for magnetization averages and fluctuations and explain how we extract T_c from them. We then proceed with some technical considerations that en-

ter into these calculations before summarizing the numerical results we have obtained to date.

1. Magnetisation curves and fluctuations

Figure 1 shows typical magnetisation data as a function of the temperature. These results were obtained for a manganese ion density of $N = 1.0\text{nm}^{-3}$, a carrier density $n = 0.1\text{nm}^{-3}$ in a cubic simulation volume of $V = 540\text{nm}^3$, i. e. the system contains 540 manganese ions and 54 carriers. The effective band mass is half the bare electron mass, and the exchange parameter is $J_{pd} = 0.15\text{eVnm}^3$. The main panel shows the average polarisation of the manganese spins,

$$M = \frac{1}{NV} \langle |\vec{S}_{tot}| \rangle, \quad (18)$$

i. e. the thermally averaged modulus of the total ion spin, along with the carrier magnetisation,

$$m = \frac{1}{nV} \langle |\langle 0 | \vec{s}_{tot} | 0 \rangle| \rangle, \quad (19)$$

which is the ensemble average of the modulus of the total ground-state carrier spin. Both quantities are divided by the number of particles and are close to their maximum values at low temperatures. At higher temperatures they show the expected transition to a paramagnetic phase. The critical temperature of this ferromagnetic transition is most readily estimated from numerical results for the magnetisation fluctuations:

$$g_{Mn} = \frac{1}{NV} \left(\langle |\vec{S}_{tot}|^2 \rangle - \langle |\vec{S}_{tot}| \rangle^2 \right), \quad (20)$$

$$g_p = \frac{1}{nV} \left(\langle |\langle 0 | \vec{s}_{tot} | 0 \rangle|^2 \rangle - \langle |\langle 0 | \vec{s}_{tot} | 0 \rangle| \rangle^2 \right). \quad (21)$$

These two fluctuations per particle are plotted in the insets of Fig. 1. They both show a pronounced peak at a temperature $T \sim 100\text{K}$, defining the finite-system transition temperature for these model parameter values. In fact, in a region around this transition both datasets differ just by a factor of approximately 25, which is the square of the ratio of the two spin lengths entering the expressions (20) and (21), respectively. This observation shows explicitly that the correlation length both for the manganese ions and in the carrier system is the same near the transition, namely given essentially by the system size.

In conclusion, our Monte Carlo approach clearly reproduces the expected ferromagnetic transition. The transition temperature T_c can be determined unambiguously and consistently from the positions of very pronounced peaks in total magnetisation fluctuations of both the Mn ions and the carriers.

2. Technical Considerations

(i) **Monte Carlo parameters and disorder realisations.** The data of Fig. 1 was obtained by averaging over five different realisations of the manganese-ions. For each Monte Carlo run the system was thermalized within the first 1000 accepted steps, and the subsequent measurement phase included 10000 accepted steps. The Hamilton equations of motions (12) are integrated over an interval of length 1 in each Monte Carlo step. These simulation parameters were used for all results reported in this paper. After the first 1000 steps the magnetisations for the five different systems differ only by a few percent. This indicates that the thermalization phase was long enough. In fact, for not too large density ratios n/N , the final results for the different disorder realisations differ only very weakly from each other. This is illustrated in Fig. 2, where the magnetisation curves underlying the averaged results of Fig. 1 are plotted. Those five datasets are hardly distinguishable from each other.

(ii) **Wavevector cutoff.** Periodic boundary conditions restrict wavevector components for the carriers to integer multiples of $2\pi/L$, where $L = V^{1/3}$ is the edge length of the simulation cube. In our numerical calculations we include wavevectors \vec{k} up to a certain cutoff k_c . For the single-parabolic band model the wavevector cutoff corresponds simply to a kinetic-energy cutoff. The wavevector cutoff has to be chosen carefully, since our results are most cleanly interpreted when their cutoff dependence has been saturated. On the other hand the dimension of the single-particle Hamiltonian matrices, whose construction limits our numerical calculations, grows with the third power of the cutoff. Fortunately, our data converge comparatively quickly with the cutoff parameter. Figure 3 shows magnetization curves for the same system parameters as in Fig. 1 (but in a smaller simulation cell of volume $V = 140\text{nm}^3$) for two different cutoff parameters. In the first case, $k_c = 2(2\pi/L)$ and the single-particle Hilbert space for the 14 carriers has dimension 66 (including the spin degree of freedom), while in the second case, $k_c = \sqrt{6}(2\pi/L)$ and the dimension increases to 162. The datasets shown in Fig. 3 are very close to each other over a large temperature range around the ferromagnetic transition. This demonstrates that the smaller cutoff is already sufficient (nevertheless we used the larger one for Fig. 1). In the simulations of larger systems with more carriers the cutoff parameter is appropriately adjusted.

(iii) **Finite-size effects.** The finite size of the simulation cell implies that the set of fermion energies obtained for a particular Mn spin orientation configuration is discrete. The gaps between adjacent energy eigenvalues depends on the size of the simulation cube and may lead to systematic \vec{k} -space shell effects in the model's finite-size dependence. These are less important at temperatures of interest, since the typical orientation configuration is complex and produces an exchange field that removes all

degeneracies and smears the \vec{k} -space shells. Shell effects are therefore more important for weaker exchange coupling, limiting our ability to do reliable calculations in the weak-coupling limit. As we discuss later, however, we believe that mean-field theory tends to be reliable in this limit, reducing the motivation for Monte Carlo studies. Nevertheless, finite-size effects can be observed at all coupling strengths. Their character is easily understood by recognizing that Mn spins are coupled by the polarization they produce in the electron system. When a \vec{k} -space shell is partially filled, its degeneracy is lifted by exchange coupling with a Mn spin-configuration. Occupying the lower energy states in the split multiplet produces a larger electron spin polarization than when the multiplet is full. Of course these effects become less important at larger system sizes when the typical level shift is much larger than the typical level spacing. The ferromagnetic transition temperature has systematic minima for the closed-shell ‘magic’ electron numbers at which most of our simulations are performed. This effect becomes smaller with increasing system size. Figure 4 shows magnetisation curves for the same densities and system parameters as in Fig. 1 for systems with 14, 38, 54, and 30 carriers. The first three carrier numbers correspond to “closed shell” configurations in the paramagnetic phase while the last one lies in between. The comparison of the data for the three largest carrier numbers shows that the finite-size effect has already become weak for carrier numbers $nV \gtrsim 30$, while the magnetisation curve for the system of 14 carriers shows slightly larger values at given temperature. However, the finite-size critical temperature obtained in this case lies only by about 15K above the values for the other three system sizes.

(iv) **The regularisation parameter a_0 .** As mentioned above we have chosen the regularisation parameter in the exchange coupling (2) to be $a_0 = 0.1\text{nm}$. This seems to be a reasonable value compared with the lattice constant of GaAs. Figure 5 shows the magnetisation data for the same system parameters as in Fig. 1 and a simulation volume of $V = 140\text{nm}^3$ for different values of a_0 . The data for $a_0 = 0.1\text{nm}$ and $a_0 = 0.2\text{nm}$ are almost identical. For larger values of a_0 a slight departure sets in. As a consequence, our results are practically independent of a_0 over the (physically motivated) range of considered values.

In summary, we have demonstrated that our Monte Carlo results are stable with respect to the influence of the wavevector cutoff and the finite system size. Moreover, the effect of different disorder realisations and the precise value of the regularisation parameter of the exchange coupling is found to be very weak.

3. Results for T_c

We now turn to the transition temperature T_c for the parabolic band model (1). Within mean field theory [6–8]

this quantity is given by

$$T_c^{MF} = \frac{\chi_P}{(g^* \mu_B/2)^2} \frac{S(S+1)N J_{pd}^2}{12}, \quad (22)$$

where $S = 5/2$ is the spin length of the manganese ions, and g^* is the g-factor of the carriers. Their Pauli susceptibility χ_P reads

$$\chi_P = \frac{3}{2} \frac{n}{\varepsilon_F} (g^* \mu_B/2)^2 \quad (23)$$

and is via the Fermi energy ε_F proportional to the effective mass m^* .

The above expression for T_c can be obtained by averaging the ion-spin and carrier polarization over space. The effective field which each manganese spin experiences due to a finite carrier polarization is constant in space and the carrier bands are in turn spin split by $\Delta = J_{pd}NS$ by a spatially homogeneous effective magnetic field. (The limit in which mean-field theory is exact can be achieved in our model by letting $a_0 \rightarrow \infty$ in Eq. (2).) In this very simplified approach, spatial fluctuations and correlations between carriers and manganese spins are neglected. As a result, mean-field theory predicts T_c to be quadratic in the exchange parameter J_{pd} and linear in the effective band mass m^* . This mean-field theory has been used to predict values for T_c in various semiconductor host materials [6]. It is, however, expected [11,12] that due to the neglect of correlations, Weiss mean-field theory can substantially overestimate the critical temperature.

We, therefore, investigate the critical temperature T_c with the help of our Monte Carlo scheme. As seen in Fig. 1 this quantity can be read off unambiguously from the magnetic fluctuations of both the Mn ions and the carriers. To limit computational expense we concentrate on systems with fourteen carriers. From Fig. 4 we conclude that finite-size effects will lead to values of T_c which are only slightly too large (less than 20K). Furthermore, the *qualitative* behavior of the T_c data as a function of system parameters such as the effective mass m^* will not be affected by the finite simulation-cell size.

In Fig. 6 we show results for a manganese densities $N = 1.0\text{nm}^{-3}$ and a mean-field band splitting $\Delta = J_{pd}NS = 0.5\text{eV}$. The left panel shows the dependence of the critical temperature on the carrier effective mass. This dependence is very important for the search for diluted magnetic semiconductor systems with T_c ’s larger than room temperature. In the mean-field approximation, T_c grows linear with increasing mass. The Monte Carlo results clearly deviate from this prediction suggesting a saturation of T_c at carrier masses close to the bare electron mass. For even higher masses, we expect the electrons to behave more classically and localize around individual Mn spins. The cost in electronic energy of changing relative orientations of nearby Mn spins will get smaller causing T_c to decline and eventually causing ferromagnetism to disappear. This physics also occurs in a continuum model where the spin stiffness declines as

$1/m^*$ for large band masses [11,12], although there are differences in detail.

To discuss the critical temperature as a function of the exchange coupling parameter J_{pd} we observe that the Hamiltonian (1) satisfies the scaling relation

$$\beta\mathcal{H}(m^*, J_{pd}) = \frac{\beta}{q}\mathcal{H}\left(\frac{m^*}{q}, qJ_{pd}\right) \quad (24)$$

with $q > 0$. Therefore the saturation of T_c as a function of the effective mass at fixed J_{pd} corresponds to a linear dependence of T_c on J_{pd} at fixed m^* . This contrasts with the mean-field prediction $T_c^{MF} \propto J_{pd}^2$.

In the right panel of Fig. 6 we show T_c as a function of the carrier density. Here the Monte Carlo approach also clearly yields a lower critical temperatures than mean-field theory. For still higher carrier densities the typical distance between nearby Mn ions will become larger than the band electron Fermi wavelength, causing the sign of the typical exchange coupling to oscillate in an RKKY fashion. We expect the resulting frustration to make the ferromagnetic state unstable, possibly leading to a regime of spin-glass order.

As discussed above, different disorder realisations with respect to the ion positions give almost identical critical temperatures (see also Fig. 2). This does not mean, however, that the presence of disorder is unimportant. Numerical finite-size studies at $T = 0$ have shown that in the limit of strong exchange coupling J_{pd} the presence of disorder increases the spin stiffness [12,22] for the regime of densities and masses covered by our calculations. This, in turn, enhances the critical temperature since, according to analytical estimates from spin-wave theory, T_c is approximately proportional to the spin stiffness [12]. On the other hand, our Monte Carlo results show that the spin stiffness enhancement does not depend on the concrete disorder realization.

4. Local vs. global polarisation

In mean-field theory, the free carrier band spin-splitting vanishes as the critical temperature is approached. This is, however, not generally the correct physical picture. When long-wavelength collective fluctuations [11,12], which are neglected by mean-field theory, drive the breakdown of ferromagnetism the *local* carrier spin polarization can remain finite even above T_c . Ferromagnetism and the *global* spin polarization disappears only because of the loss of long-range spatial coherence. The applicability of this picture to the studied parameter ranges of the kinetic exchange model is confirmed by our Monte Carlo studies. In Fig. 7 we compare the global (Eq. (19)) and local carrier spin polarizations,

$$m_{loc} = \left\langle \frac{|\vec{s}(\vec{r})|}{n(\vec{r})} \right\rangle, \quad (25)$$

which is the thermally and spatially averaged ratio of the *modulus* of the carrier spin density $\vec{s}(\vec{r})$ and the local carrier density $n(\vec{r})$. The system parameter are the same as in Fig. 1. While the global spin polarization vanishes at the critical temperature, the local polarization remains finite and saturates at about forty percent of its $T = 0$ value.

B. Six-band model

We now turn to the six-band model in which the kinetic energy part is given by the Kohn-Luttinger Hamiltonian (4). To model GaAs we use $(\gamma_1, \gamma_2, \gamma_3) = (6.85, 2.1, 2.9)$ for the Luttinger parameters, and the spin-orbit coupling energy is $\Delta_{so} = 0.34\text{eV}$.

Figure 8 shows typical magnetisation data for a system with exchange coupling $J_{pd} = 0.15\text{eVnm}^3$, carrier density is $n = 0.1\text{nm}^{-3}$, and Mn ion density $N = 1.0\text{nm}^{-3}$ in a volume of $V = 280\text{nm}^3$. As in the case of parabolic bands, a ferromagnetic transition is clearly signalled by pronounced peaks in the magnetic fluctuations of both Mn ions and carriers. We find that, in contrast to the parabolic two-band model, the carrier magnetisation is already reduced at temperatures well below T_c . Another difference compared to the parabolic-band model concerns the shape of the magnetic fluctuations for the manganese ions and the carriers as a function of temperature. Although both curves indicate the same value for T_c , their shape in the vicinity of T_c is slightly different and the ratio of the their fluctuations is smaller than 25 (the square of the ratio of spin lengths involved). These differences arise because of the more complicated band structure and the spin-orbit coupling present in the Kohn-Luttinger Hamiltonian.

As for the two-band model, the data shown in Fig. 8 are the average over five different disorder realisations. Also in the present case, the dependence of the data on the concrete realisation is very weak. Moreover, we again find that the local carrier polarization remains finite above T_c while the global magnetization vanishes.

In the right panel Fig. 9 we plot the transition temperature as a function of the exchange coupling J_{pd} for two different system sizes. Both data sets agree within error bars and show a linear dependence of T_c on J_{pd} . This finding is the same as for the two-band model and contrasts with mean-field theory which predicts $T_c \propto J_{pd}^2$. The left panel of Fig. 9 shows the transition temperature as a function of J_{pd} for the parabolic model for an effective mass $m^* = 0.5m$. This value is close to the heavy-hole mass in the Kohn-Luttinger model for parameters appropriate for GaAs as given above. The data in the left panel can be obtained from the left panel of Fig. 6 via the scaling relation (24). Comparing the two panels of Fig. 9 demonstrates that, in the range of carrier densities studied, a single parabolic band with an effective mass close to that of the heavy-hole Kohn-Luttinger-

model band provides a reasonably good approximation to the behavior of the six-band system.

V. SUMMARY

We have given a detailed report on Monte Carlo studies of (III,Mn)V ferromagnetic semiconductors. We use a kinetic-exchange model in which localized magnetic moments formed by Mn ions are coupled antiferromagnetically to carriers (holes) in the valence band. In most of our simulations we describe the valence-band carriers by simple parabolic bands but we investigate a model with a refined six-band $\vec{k} \cdot \vec{p}$ model as well. We treat the manganese spins as classical magnetic moments, and take the carriers effectively at zero temperature. Both approximations are comparatively weak. Our treatment accounts for spatial fluctuations in the magnetization and for disorder induced by the randomness of the Mn ion positions, effects which are both neglected in a mean-field description.

We outline the Hybrid Monte Carlo algorithm employed and discussed its advantages compared to other methods. A complete account of important technical details of the computation is given. We have shown that the effects of different disorder realizations, wavevector cutoff, and finite-size effects are well under control. Our results do almost not depend on the regularization parameter a_0 which described the spatial range of the exchange mechanism between carriers and ions.

We find that due to spatial fluctuations and correlations the total magnetization and therefore also the ferromagnetic transition temperature T_c is considerably reduced in comparison to mean-field estimates. Furthermore, we proved that in contrast to mean-field predictions T_c is not a linear function of the effective band mass and is not proportional to the square of the exchange coupling constant. The discrepancy becomes more severe the higher the value of the predicted mean-field critical temperature is.

The importance of spacial fluctuations of the magnetization neglected in a mean-field description is, furthermore, emphasized by the fact that the local carrier spin polarization remains finite even well above the ferromagnetic transition temperature.

ACKNOWLEDGMENTS

We thank Glenn Martyna for bringing the advantages of the Hybrid Monte Carlo algorithm to our attention, and M. Abolfath, A. Burkov, T. Jungwirth, B. Lee, H. H. Lin, and Y. Sato for useful discussions. J. S. and J. K. were supported by the Deutsche Forschungsgemeinschaft. A. H. M. was supported by the National Science Foundation. We also acknowledge support by the Indiana 21st Century Fund.

-
- [1] J. K. Furdyna, J. Kossut, *Diluted Magnetic Semiconductors*, in *Semiconductors and Semimetals*, volume 25, Academic Press (1988); T. Dietl, *Diluted Magnetic Semiconductors*, in *Handbook of Semiconductors*, volume 3B, North-Holland (1994).
 - [2] H. Ohno, A. Shen, F. Matsukura, A. Oiwa, A. Endo, S. Katsumoto, Y. Iye, Appl. Phys. Lett. **69**, 363 (1996).
 - [3] H. Ohno, Science, **281**, 951 (1998).
 - [4] For a recent review see H. Ohno, F. Matsukura, Solid State Commun., to appear (2001).
 - [5] G. A. Prinz, Science **282**, 1660 (1998).
 - [6] T. Dietl, A. Haury, Y. M. d'Aubigné, Phys. Rev. B **55**, R3347 (1997); T. Dietl, H. Ohno, F. Matsukura, J. Cibert, D. Ferrand, Science **287**, 1019 (2000); T. Dietl, H. Ohno, F. Matsukura, cond-mat/0007190.
 - [7] M. Abolfath, T. Jungwirth, J. Brum, A. H. MacDonald, cond-mat/0006093.
 - [8] T. Jungwirth, W. A. Atkinson, B. H. Lee, A. H. MacDonald, Phys. Rev. B **59**, 9818 (1999); B. H. Lee, T. Jungwirth, A. H. MacDonald, Phys. Rev. B **61**, 15606 (2000).
 - [9] S. Sanvito, P. Ordejon, N. A. Hill, cond-mat/0011050; S. Sanvito, N. A. Hill, cond-mat/0011372.
 - [10] T. C. Schulthess, W. B. Butler, private communication (2000).
 - [11] J. König, H. H. Lin, A. H. MacDonald, Phys. Rev. Lett. **84**, 5628 (2000); to appear in "Interacting Electrons in Nanostructures", edited by R. Haug and H. Schoeller (Springer), cond-mat/0010471.
 - [12] J. Schliemann, J. König, H. H. Lin, A. H. MacDonald, cond-mat/0010036.
 - [13] S. Duane, A. D. Kennedy, B. J. Pendleton, D. Roweth, Phys. Lett. B **195**, 216 (1987).
 - [14] O. Sakai, S. Suzuki, K. Nishizawa, preprint (2000).
 - [15] X. Wan, R. N. Bhatt, cond-mat/0009161; R. N. Bhatt, M. Berciu, cond-mat/0011319.
 - [16] R. Car, M. Parrinello, Phys. Rev. Lett. **55**, 2471 (1985); G. Galli, M. Parrinello in *Computer Simulations in Materials Science*, M. Meyer, V. Pontikis (eds.), Kluwer (1991); P. E. Blöchl, M. Parrinello, Phys. Rev. B **45**, 9413 (1992).
 - [17] A. K. Bhattacharjee, C. Benoit à la Guillaume, Solid State Comm. **113**, 17 (2000).
 - [18] W. W. Chow, S. W. Koch, *Semiconductor-Laser Fundamentals*, Springer (1999).
 - [19] J. M. Luttinger, W. Kohn, Phys. Rev. **97**, 869 (1955).
 - [20] For a recent review see I. Vurgaftman, J. R. Meyer, L. R. Ram-Mohan, Appl. Phys. Rev. (in press).
 - [21] J. A. Alonso, L. A. Fernandez, F. Guinea, V. Laliena, V. Martin-Mayor, cond-mat/0007450.
 - [22] J. König, J. Schliemann, A. H. MacDonald, unpublished.

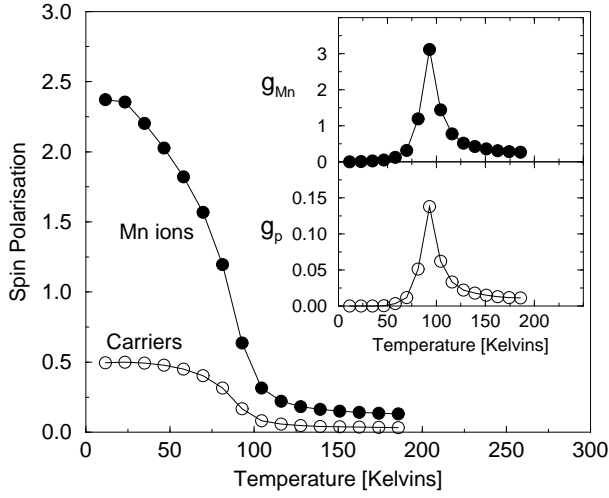


FIG. 1. Magnetization curves for manganese ions and carriers. The upper and lower inset show the magnetic fluctuations for the manganese ions and the carriers, respectively. Both differ by a factor of approximately 25 reflecting the square of the ratio of spin lengths. The density of manganese ions is $N = 1.0\text{nm}^{-3}$, the carrier density is $n = 0.1\text{nm}^{-3}$ in a cubic volume of $V = 540\text{nm}^3$. The band mass is half the bare electron mass with an exchange parameter of $J_{pd} = 0.15\text{eVnm}^3$.

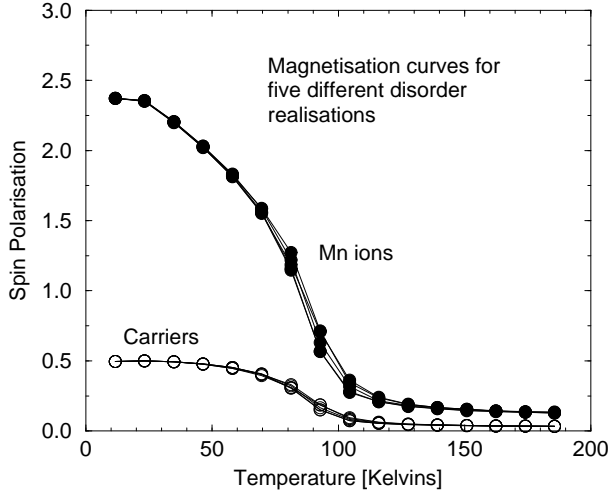


FIG. 2. Magnetisation curves for five different realisations of manganese positions underlying the averaged data of Fig. 1.

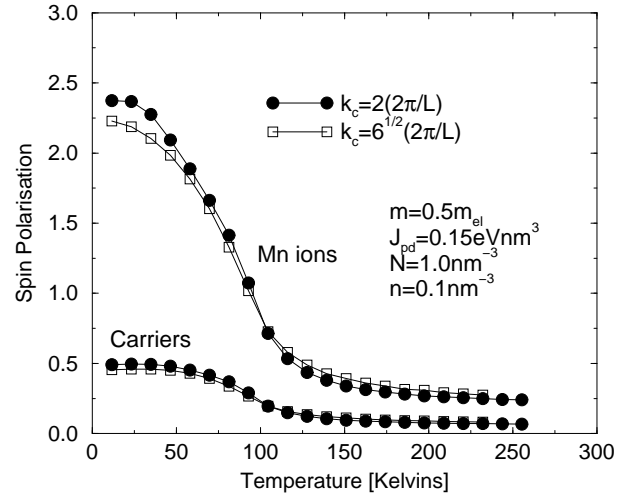


FIG. 3. Magnetisation data for the same system parameters as in Fig. 1 in a cubic volume of $V = 140\text{nm}^3$ for two different values of the wavevector cutoff. In a large area around the ferromagnetic transition both datasets are very close to each other.

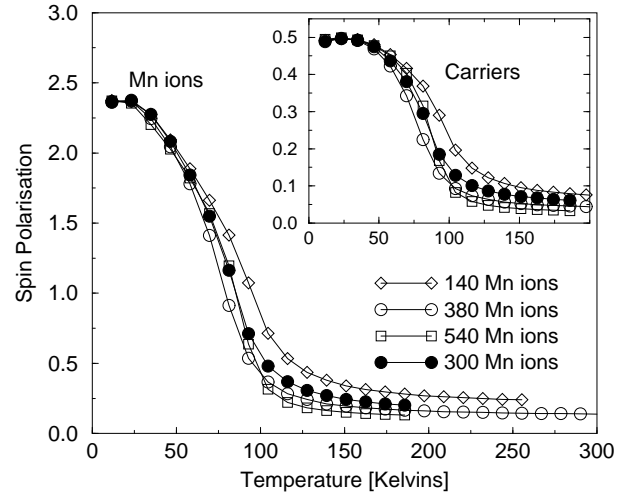


FIG. 4. Magnetisation data for the same densities and band mass and exchange parameter as in Fig. 1 for different system sizes. The first three systems with 14, 38, and 54 carriers correspond to “closed shell” configurations in the paramagnetic carrier state, while the last system (30 carriers) lies in between.

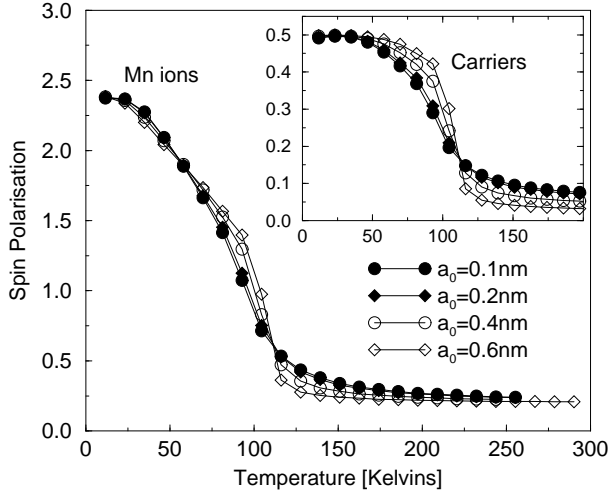


FIG. 5. Magnetisation data for the same system parameters as in Fig. 1 in a cubic volume of $V = 140\text{nm}^3$ for different values of the regularisation parameter a_0 . At not too large values for a_0 the dependence on this quantity is extremely weak.

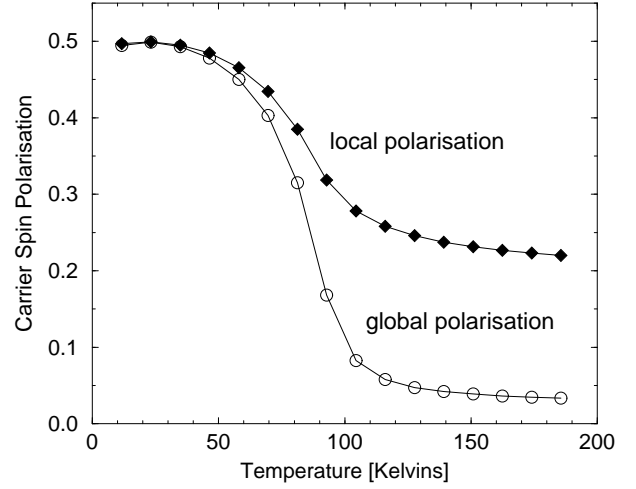


FIG. 7. Local versus global carrier spin polarisation for the same system as in Fig. 1 as a function of temperature. The local carrier polarisation remains finite above T_c .

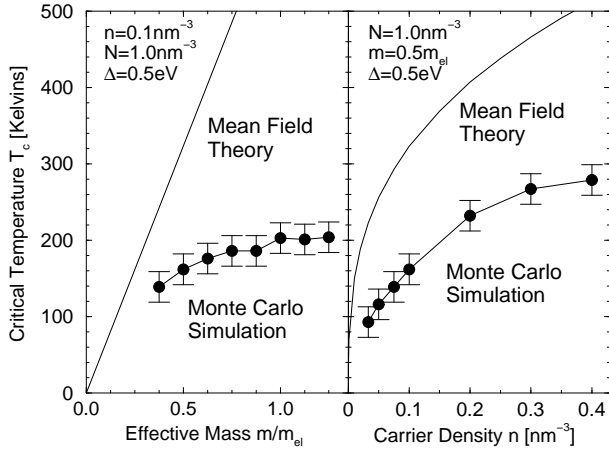


FIG. 6. The critical temperature T_c as a function of the carrier mass (left panel) and the carrier density (right panel). The results of the Monte Carlo runs are compared with the mean-field predictions.

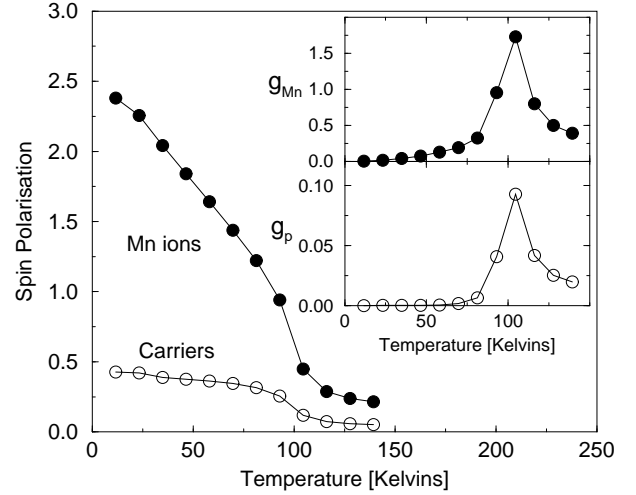


FIG. 8. Magnetisation curves for Mn ions and carriers in the six-band model for n exchange coupling of $J_{pd} = 0.15\text{eVnm}^3$. The carrier density is $n = 0.1\text{nm}^{-3}$ with an Mn ion density of $N = 1.0\text{nm}^{-3}$ in a volume of $V = 280\text{nm}^3$. As in the case of parabolic bands, the ferromagnetic transition is clearly and consistently signalled by pronounced peaks in the magnetic fluctuations shown in the insets.

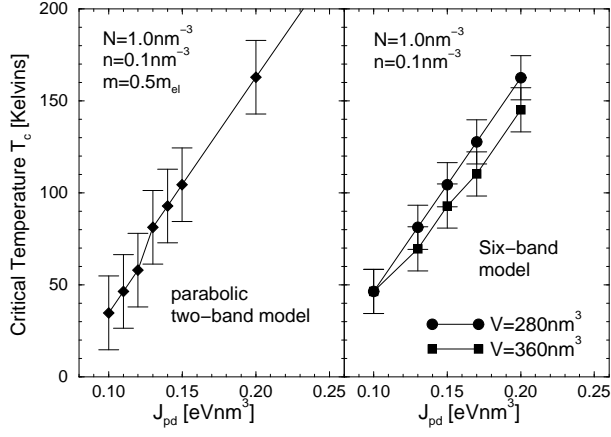


FIG. 9. The right panel shows critical temperature T_c as a function of the exchange parameter J_{pd} for the same particle densities as in Fig. 8 and two different system sizes. Both data sets agree within error bars and show a linear dependence of T_c on J_{pd} . In the left panel, the corresponding data for the parabolic two-band model with an effective mass of half the bare electron mass is plotted. The latter system is a reasonable approximation to the six-band case.